GeoHazards

MDPI

*Article*

# Analysis of Fault Slip Potential of Seismogenic Faults Based on In Situ Stress Measurement and Monitoring Data—A Case Study of the Strong Seismic Region in Zhangbei, North China

**Jing Meng [1,2], Yulu Fan [1,2,*], Chengjun Feng [1,2], Peng Zhang [1,2], Bangshen Qi [1,2] and Chengxuan Tan [1,2]**

[1] Institute of Geomechanics, Chinese Academy of Geological Sciences, Beijing 100081, China; mexijay@sina.com (J.M.); feng2010618@aliyun.com (C.F.)
[2] Key Laboratory of Active Tectonics and Geological Safety, Ministry of Natural Resources, Beijing 100081, China
* Correspondence: fanfyl@163.com

**Abstract**

The aim of this paper is to investigate dynamic adjustment of the in situ stress field and the stability of main faults in the Zhangbei strong seismic region. Firstly, we utilized in situ stress measurement and monitoring data to discuss the dynamic adjustment process of the in situ stress field. Subsequently, the Fault Slip Potential (FSP) v.1.0 software package was employed to calculate the fault slip potential of the main faults. Finally, the potential hazard of fault activity was assessed. The conclusions are as follows. (1) Since November 2015, the in situ stress field has been primarily influenced by NEE compressive tectonic action, with a slight enhancement in the near SN compressive tectonic action. (2) In the initial stage, NE-trending faults exhibited the highest stress accumulation levels, with near-EW-trending faults the lowest. Influenced by the enhanced near-SN-trending compressive action, as of 19 October 2020, near-EW-trending faults displayed the highest stress accumulation, followed by NW-trending faults, with NE-trending faults showing the least accumulation. (3) From November 2015 to October 2020, the in situ stress field was in a continuous accumulation process. Using the Shangyi–Pingquan fault as a boundary, fault activity in the southern part of the strong seismic region is more hazardous than that in the northern part.

**Keywords:** Zhangbei strong seismic region; in situ stress monitoring; in situ stress field fault slip potential; fault stability

Check for updates

Academic Editor: Dimitrios Papanikolaou

Received: 26 January 2026
Revised: 5 April 2026
Accepted: 12 April 2026
Published: 15 April 2026

**Copyright:** © 2026 by the authors. Licensee MDPI, Basel, Switzerland. This article is an open access article distributed under the terms and conditions of the Creative Commons Attribution (CC BY) license.

## 1. Introduction

It is generally believed that earthquakes are mainly caused by the long-term accumulation, strengthening, and sudden release of strain energy in existing fault sections within a region [1]. The dynamic adjustment of the regional in situ stress field is a major factor affecting the stability of fault structures [2]. Conducting in situ stress measurements and analyzing the characteristics of the regional in situ stress field are of great scientific significance for ensuring regional geological safety. Previous studies have contributed significantly to this field [3–6]. Tanaka [7] analyzed the potential influence of original ground stress on fault slip by calculating the ratio of maximum shear stress to average stress using in situ stress measurement data. He found that this ratio increased to 0.53 before the 1995 earthquake in southeastern Hyogo Prefecture and decreased to 0.2 afterward. Townend and Zoback [8] calculated the friction coefficient of the San Andreas fault using in situ stress measurement data, finding that it was about 0.6 in the shallow part and about

0.2 in the deep part of the drilling hole. Tan et al. [9] conducted a comparative analysis of in situ stress measurement and real-time monitoring data at different key structural locations around Beijing, discovering abnormal tectonic activity in the Tangshan–Luanxian–Changli area. Feng et al. [10] used in situ stress measurement data from the Ming Tombs Station in Changping, Beijing, to calculate stress states around boreholes and adjacent areas at different periods and discussed the activity of the Nankou Piedmont fault using the Mohr–Coulomb fracture criterion and Byerlee's Law. Qiu et al. [11] evaluated the stress accumulation level and earthquake hazard in the southwestern section of the Longmenshan fault zone after the Lushan *Ms* 7.0 earthquake on 20 April 2013 using in situ stress measurement data and Byerlee's Law. Their results indicate increased stress accumulation in the northern and southern sections of the southwest Longmenshan fault zone, particularly in the northern section. The current analysis of fracture stability using in situ stress data is primarily based on calculating the friction coefficient of the fault surface according to the Mohr–Coulomb fracture criterion and Byerlee's Law in order to assess the level of stress accumulation along faults.

The Zhangbei strong seismic region is located northwest of Beijing at the intersection of the Zhangjiakou–Bohai seismic tectonic zone and the Shanxi graben zone. This area is characterized by a complex tectonic environment, frequent minor earthquakes, and occasional moderate to strong earthquakes. In January 1998, a magnitude 6.2 earthquake caused significant casualties and property losses in the local and surrounding areas. The Zhangbei strong seismic region is one of the three major earthquake-active areas surrounding the capital region of China (the other two strong seismic region are Tangshan and Xingtai), significantly impacting its structural stability. Despite its importance, there has been limited research on the tectonic stability of the Zhangbei strong seismic region, particularly concerning the dynamic adjustment of the in situ stress field and fault stability.

This paper uses in situ stress measurement data from the Zhangbei In Situ Stress Monitoring Station (hereinafter referred to as Zhangbei Station) and monitoring data from 4 November 2015 to 19 October 2020 to analyze the dynamic adjustment process of the in situ stress field in the Zhangbei strong seismic region. The Fault Slip Potential (FSP) v.1.0 software package was employed to analyze the dynamic changes in fault stability and the potential for fault instability under the current in situ stress environment, considering the uncertainties (or errors) of fault attribute parameters and in situ stress fields. It should be noted that the software's analysis results cannot be directly used for earthquake prediction, as they are mainly used to assess the level of the stress accumulation in the fault. This research aims to provide scientific support for ensuring the geological safety of China's capital region and exploring the application of real-time in situ stress monitoring in structural stability evaluation.

The FSP v.1.0 software package, developed by the Stanford Center for Induced and Triggered Seismology, is a freely available tool that allows users to estimate changes in fault slip potential based on Mohr–Coulomb criteria and Byerlee's Law [12].

## 2. Regional Geological Setting

The Zhangbei strong seismic region is tectonically situated on the northern edge of the North China Block (Figure 1) at the intersection of the Zhangjiakou–Bohai active tectonic belt and the Shanxi graben belt. The active structures in this area are well-developed, leading to frequent seismic activities [13,14].

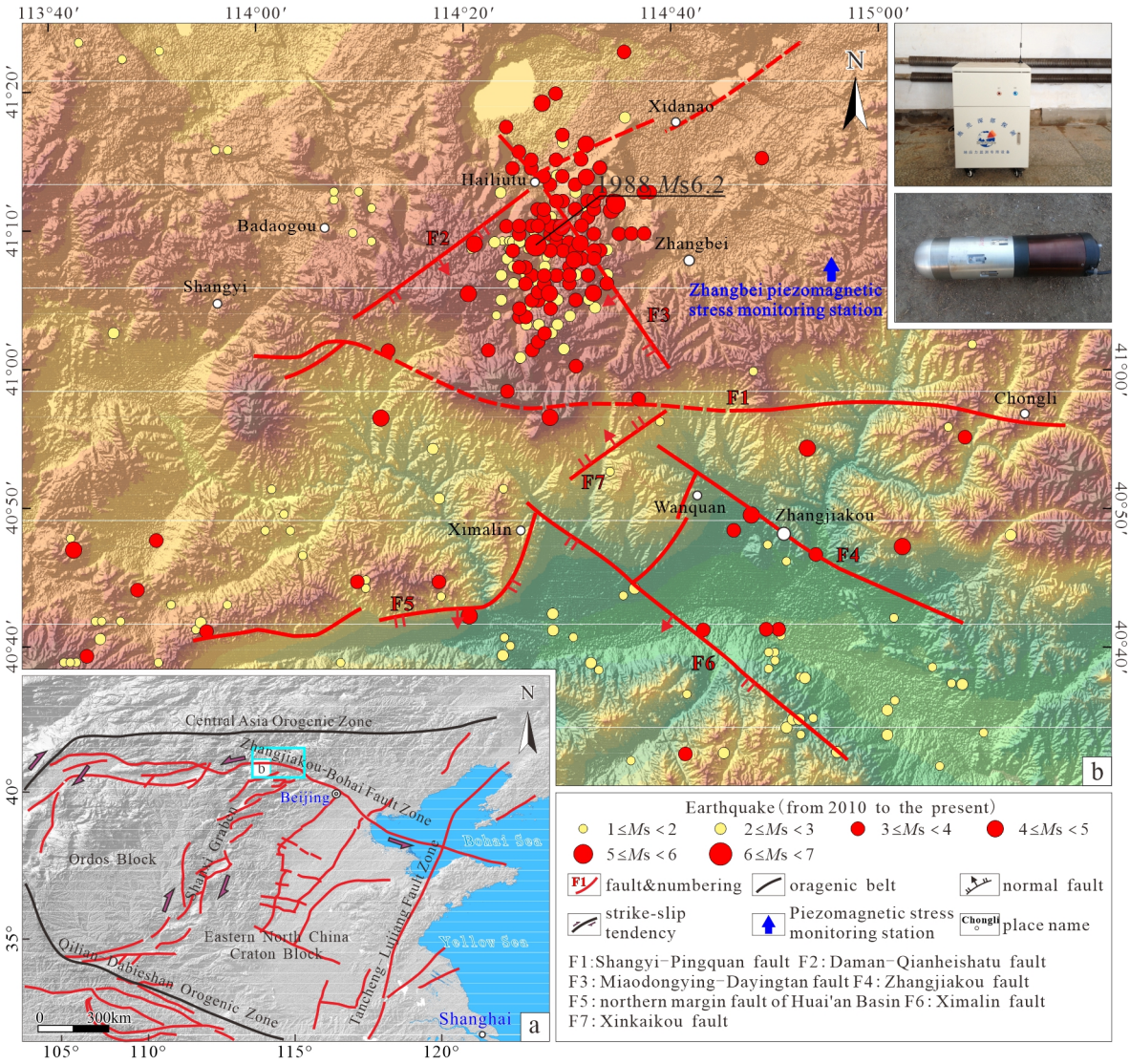



**Figure 1.** Diagram of the regional geological structure of the Zhangbei strong seismic region. (**a**) Geological structure of North China; (**b**) Geological tectonic map of Zhangbei strong seismic region.

The fault geometry in the Zhangbei strong seismic region is complex, with faults primarily trending NE-NEE and NW-NWW and a smaller number of near-EW-trending faults. Among these, the NE-NEE-trending faults are extensive and long, while the NW-NWW-trending faults have poor continuity and are mostly hidden. The main EW-trending faults include the Shangyi–Pingquan fault (F1), while the NE-NEE-trending faults primarily consist of the Daman–Qianheishatu fault (F2), the northern margin fault of the Huaian Basin (F5), and the Xinkaikou fault (F7). The NW-NWW-trending faults mainly include the Miaodongying–Dayingtan fault (F3), the Zhangjiakou fault (F4), and the Ximalin fault (F6). Detailed information on these faults is presented in Table 1 [15–19].

The Zhangbei strong seismic region is one of the most seismically active regions in North China. From 1970 to 2020, earthquake monitoring records detected a total of 418 earthquakes within the Zhangbei strong seismic region (113.65–115.35° E, 40.5–41.45° N). These events were predominantly small earthquakes (M < 3.0), including 50 earthquakes with $0.0 \leq M < 1.0$, 145 earthquakes with $1.0 \leq M < 2.0$, 87 earthquakes with $2.0 \leq M < 3.0$, 107 earthquakes with $3.0 \leq M < 4.0$, 27 earthquakes with $4.0 \leq M < 5.0$, 1 earthquake with $5.0 \leq M < 6.0$, and 1 earthquake with $6.0 \leq M < 7.0$. The seismic events were mainly concentrated at the intersection of the Daman–Qianheishatu Fault and the Miaodongying–

Dayingtan Fault, as well as in the southern part of the strong seismic region. Statistics on these earthquake events indicate that tectonic activity remains vigorous in the Zhangbei strong seismic region.

**Table 1.** List of fault characteristics in the Zhangbei strong seismic region.

| Fault Number | Fault Name | Strike | Dip Direction | Dip (°) | Fault Activity | Faulting Era |
|---|---|---|---|---|---|---|
| F1 | Shangyi–Pingquan fault | Near EW | S/N | 60~80 | Thrust/normal fault–strike slip | Q4 |
| F2 | Daman–Qianheishatu fault | NE | SE | 60~80 | Normal fault | Q4 |
| F3 | Miaodongying–Dayingtan fault | NW | SW | 75~80 | Normal fault | Q4 |
| F4 | Zhangjiakou fault | NWW | S/N | 60~80 | Normal, reverse, and strike–slip fault | Q4 |
| F5 | The northern margin fault of Huaian Basin | NEE | SE | 50~75 | Normal fault | Q4 |
| F6 | Ximalin fault | NWW | SW | 75~80 | Normal fault | Q3 |
| F7 | Xinkaikou fault | NE | NW | 60~70 | Normal fault | Q3 |

## 3. Description of Monitoring and Analysis Methods

### *3.1. Hydraulic Fracturing In Situ Stress Measurement*

Hydraulic fracturing (HF) is one of the in situ stress measurement methods recommended by the International Society for Rock Mechanics (ISRM) Commission on Testing Methods, offering advantages such as operational simplicity, applicability at great depths, reliable data, and good repeatability [20–23]. The formula version adopted in this article is Hubbert–Willis, and the method is formulated on the basis of elastic theory and relies on three fundamental assumptions: (1) the rock mass behaves as a linear–elastic, isotropic medium; (2) the borehole wall is intact and impermeable; and (3) one of the three principal stresses is a known vertical stress equal to the weight of the overburden. The testing procedure mainly comprises two components: the hydraulic fracturing test, which is intended to determine the magnitudes of in situ stresses, and the impression packer test, which is used to identify the orientation of the maximum principal stress.

Using the hydraulic fracturing in situ stress measurement test, three key parameters can be obtained at a given depth: the critical bursting pressure ($P_b$) at which the intact borehole wall fractures for the first time, the instantaneous shutoff pressure ($P_s$) when the fracture is in a critically closed state, and the fracture reopening pressure ($P_r$) required to reopen the fracture. Together with the pore pressure ($P_o$) in the rock mass, these parameters can be used to determine the maximum horizontal principal stresses ($S_H$) and minimum horizontal principal stresses ($S_h$) at that depth interval. The corresponding calculation formulas are as follows. The vertical stress ($S_V$) is determined by the weight of the overlying rock mass. This assumption is not only a fundamental premise of the hydraulic fracturing method recommended by the International Society for Rock Mechanics (ISRM) but also has been rigorously validated by theoretical analyses, global in situ measurements, and engineering practices [20–24]. Based on the regional geological data, the rock density in the Zhangbei seismic region is taken as 2650 kg/m$^3$:

$$S_H = 3P_s - P_r - P_o$$

$$S_h = P_s$$

### 3.2. Real-Time Monitoring Principle of In Situ Stress

The stress monitoring instrument at Zhangbei Station utilizes a piezomagnetic four-component monitoring instrument. Each component probe (P1~P4) of the instrument is positioned at a 45° angle relative to one another, enabling the generation of four sets of original monitoring data in real-time. The core component of the piezomagnetic in situ stress monitoring system is a piezomagnetic stress sensor based on the principle of magnetostriction. This sensor primarily consists of a mandrel made from a special ferromagnetic material (iron–nickel alloy) and a self-inductance coil wound around it [25–27] (Figure 2).

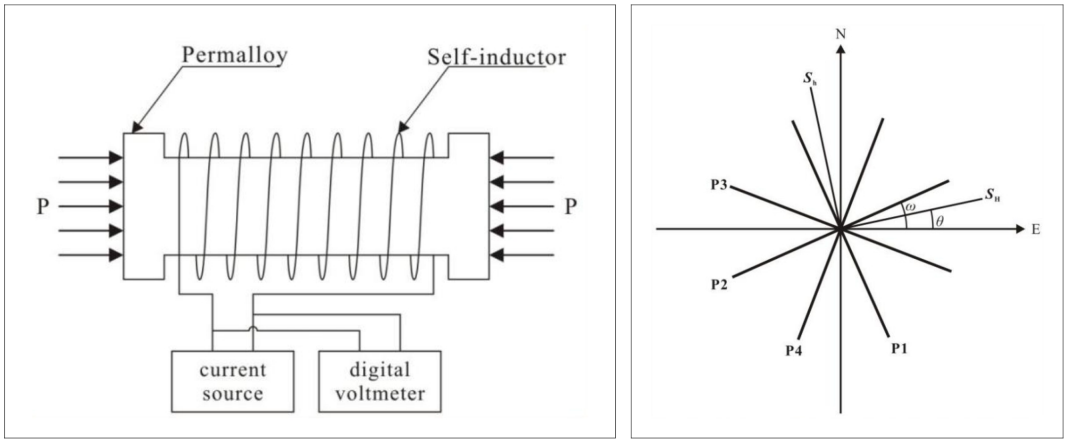



**Figure 2.** Principles of piezomagnetic stress monitoring.

The self-inductance coil is connected to a constant power supply. When an external force is applied to the ferromagnetic material, the resulting deformation of the mandrel alters the impedance value of the coil, causing a change in the coil's voltage. By monitoring these real-time voltage changes and referencing the calibration curve of indoor surrounding pressure and voltage, the stress changes acting on the measuring element in the monitoring probe can be determined.

### 3.3. Principal Stress Least Squares Solution Based on Monitoring Data

A rectangular coordinate system XOY is established, with the positive orientation of the *X*-axis oriented east and the positive orientation of the *Y*-axis oriented north. The angle between P2 and the *X*-axis is denoted as $\omega$, and the angle between the maximum horizontal principal stress and the *X*-axis is denoted as $\theta$. The changes in the normal stress at a certain time relative to the initial stage in the four monitoring orientations are represented by $\Delta\sigma_1$, $\Delta\sigma_2$, $\Delta\sigma_3$, and $\Delta\sigma_4$. Using the two-dimensional plane stress tensor transformation formula, the $S_H$ and $S_h$ values, as well as the $S_H$ orientation at any given time, can be calculated according to the following equations [28].

$$\begin{cases} \Delta\sigma_{xx} = \frac{\Delta\sigma_1+\Delta\sigma_2+\Delta\sigma_3+\Delta\sigma_4}{4} + \frac{(\Delta\sigma_1-\Delta\sigma_3)\cos 2\omega-(\Delta\sigma_2-\Delta\sigma_4)\sin 2\omega}{2} \\ \Delta\sigma_{yy} = \frac{\Delta\sigma_1+\Delta\sigma_2+\Delta\sigma_3+\Delta\sigma_4}{4} - \frac{(\Delta\sigma_1-\Delta\sigma_3)\cos 2\omega-(\Delta\sigma_2-\Delta\sigma_4)\sin 2\omega}{2} \\ \Delta\tau_{xy} = \frac{(\Delta\sigma_1-\Delta\sigma_3)\sin 2\omega+(\Delta\sigma_2-\Delta\sigma_4)\cos 2\omega}{2} \end{cases} \quad (1)$$

$$\begin{cases} S_H = \frac{(\sigma_{xx}^P+\Delta\sigma_{xx})+(\sigma_{yy}^P+\Delta\sigma_{yy})}{2} + \frac{\sqrt{(\sigma_{xx}^P+\Delta\sigma_{xx})-(\sigma_{yy}^P+\Delta\sigma_{yy})+4(\tau_{xy}^P+\Delta\tau_{xy})^2}}{2} \\ S_h = \frac{(\sigma_{xx}^P+\Delta\sigma_{xx})+(\sigma_{yy}^P+\Delta\sigma_{yy})}{2} - \frac{\sqrt{(\sigma_{xx}^P+\Delta\sigma_{xx})-(\sigma_{yy}^P+\Delta\sigma_{yy})+4(\tau_{xy}^P+\Delta\tau_{xy})^2}}{2} \\ \tan 2\theta = \frac{2(\tau_{xy}^P+\Delta\tau_{xy})}{(\sigma_{xx}^P+\Delta\sigma_{xx})-(\sigma_{yy}^P+\Delta\sigma_{yy})} \end{cases} \quad (2)$$

where $\Delta\sigma_{xx}$, $\Delta\sigma_{yy}$, and $\Delta\tau_{xy}$ are the changes in the plane stress component in the XOY coordinate system due to changes in the in situ stress field at a given time and $\sigma^{P}_{xx}$, $\sigma^{P}_{yy}$, and $\tau^{P}_{xy}$ are the plane stress components of the initial in situ stress value in the XOY coordinate system.

## 4. Dynamic Adjustment of the In Situ Stress Field

### *4.1. Characteristics of Initial In Situ Stress Field*

Zhangbei Station (41.12° N, 114.93° E) is located in Xiaoertai Township, Zhangbei County. The borehole orifice's elevation is 1495 m, with a borehole depth of 600 m. The lithology primarily consists of Mesoproterozoic mesocoarse-grained metamorphic granite, monzonite granite, and granitic gneiss. The borehole core is incomplete, and joints are relatively well-developed (Figure 3).




**Borehole Columnar Section for In-situ Stress Measurement and Real-time Monitoring in Zhangbei County, Hebei Province**

vertical scale 0 20m

Borehole ID:ZK08 | Collar elevation:1495m | Borehole diameter:75mm

Coordinates 41°07′6.″ N, 114°55′59.9″ E | Drilling date:2015.8.17–2015.10.11

| ID | Elev. (m) | base depth (m) | Thk. (m) | Lith. col. | Lithological description | RQD (%) | Rem. |
|---|---|---|---|---|---|---|---|
| 1 | 1448.89 | 47.11 | 47.11 | | Loose deposits composed of rock blocks and detrital material, representing the strongly weathered near–surface zone of the rock mass. The rock mass fabric is completely destroyed. The protolith comprises light–reddish, medium–to fine-grained Erchang granite and dark gray–black granitic gneiss. | 0.00 | Q |
| 2 | 1435.04 | 60.96 | 13.85 | | Gray, fine–grained metamorphic granite, characterized by a fine–grained granoblastic texture and massive structure; the rock is hard and slightly weathered. The core is fractured and incomplete, occurring as angular fragments. Joints are well developed, with dip angles of approximately 60°–80°. | 18.87 | |
| 3 | 1408.20 | 87.80 | 26.84 | | | | |
| 4 | 1381.37 | 114.63 | 26.83 | | Dark gray–black biotite granitic gneiss, characterized by a fine–grained granoblastic texture and gneissic foliation; the rock is hard and slightly weathered. A total of 85 joints are developed, with dip angles of approximately 45°–60°. | 30.74 | |
| 5 | 1371.76 | 124.24 | 9.61 | | Light–reddish metamorphosed medium– to coarse–grained monzogranite, characterized by a medium–to coarse–grained granoblastic texture and massive structure; the rock is hard and slightly weathered. The core is incomplete and mostly occurs as angular fragments, and joints are well developed. | 27.30 | |
| 6 | 1341.73 | 154.27 | 30.03 | | Fractured zone, the core is loose in structure. | 10.02 | |
| 7 | 1320.22 | 175.78 | 21.51 | | Light–reddish metamorphosed medium–to coarse–grained monzogranite, characterized by a medium–to coarse–grained granoblastic texture and massive structure; the rock is hard and slightly weathered. The core is incomplete and mostly occurs as angular fragments. | 10.09 | |
| 8 | 1315.51 | 180.49 | 4.71 | | | | |
| 9 | 1251.03 | 244.97 | 64.48 | | Dark gray–black biotite granitic gneiss, characterized by a fine–grained granoblastic texture and gneissic foliation; the rock is hard and slightly weathered. The core is relatively incomplete. A total of 74 joints are developed, with dip angles of approximately 45°–70°. | 45.66 | |
| | | | | | Fractured zone, the core is loose in structure. | 1.90 | |
| 10 | 1199.59 | 296.41 | 51.44 | | Dark gray–black granitic gneiss, characterized by a medium–to fine–grained granoblastic texture and gneissic foliation; the rock is hard and slightly weathered. A total of 95 joints are developed, with dip angles of approximately 45°–70°. | 20.10 | |
| | | | | | Light–reddish metamorphosed fine–grained monzogranite, characterized by a fine–grained granoblastic texture and massive structure; the rock is hard and slightly weathered. The core is incomplete and mostly occurs as angular fragments, and joints are well developed. | 38.58 | Pt:M |
| 11 | 1138.04 | 357.96 | 61.55 | | Dark gray–black granitic gneiss, characterized by a medium–to fine–grained granoblastic texture and gneissic foliation; the rock is hard and slightly weathered. The core is incomplete. A total of 104 joints are developed, with dip angles of 45°–70°. | 17.69 | |
| 12 | 1130.83 | 365.17 | 7.21 | | Fractured zone, the core is loose in structure. | 11.22 | |
| 13 | 1034.69 | 461.31 | 96.14 | | Light–reddish metamorphosed medium–to coarse–grained monzogranite, characterized by a medium–to coarse–grained granoblastic texture and massive structure; the rock is hard and slightly weathered. The core is relatively incomplete, and joints are well developed. | 26.62 | |
| 14 | 990.35 | 505.65 | 44.34 | | Dark gray–black biotite granitic gneiss, characterized by a medium–to coarse–grained granoblastic texture and gneissic foliation. the rock is hard. The core is relatively incomplete, and joints are well developed. | 11.75 | |
| 15 | 895.85 | 600.15 | 94.50 | | Light–reddish metamorphosed medium–to coarse–grained monzogranite, characterized by a medium– to coarse–grained granoblastic texture and massive structure; the rock is hard and slightly weathered. The core is relatively incomplete, and joints are well developed. | 13.76 | |

**Figure 3.** Zhangbei in situ stress measurement and real-time monitoring borehole columnar profile.

In situ stress measurements at the Zhangbei station were conducted using the hydraulic fracturing method. Based on borehole logging records and the recovered cores, a total of 12 test intervals were selected from shallow to deep for HF testing. The results (Figure 4) show well-defined pressure–time curves, with distinct inflection points corresponding to brittle rock failure, fracture reopening, and fracture closure. Guided by

the HF results, three representative intervals were further selected for impression packer tests; the impressions (Figure 5) are clear and complete, faithfully capturing the fracture characteristics. On the basis of both the HF and impression packer test data, the in situ stress magnitudes were calculated following the standard hydraulic fracturing theory, and the results are summarized in Table 2.

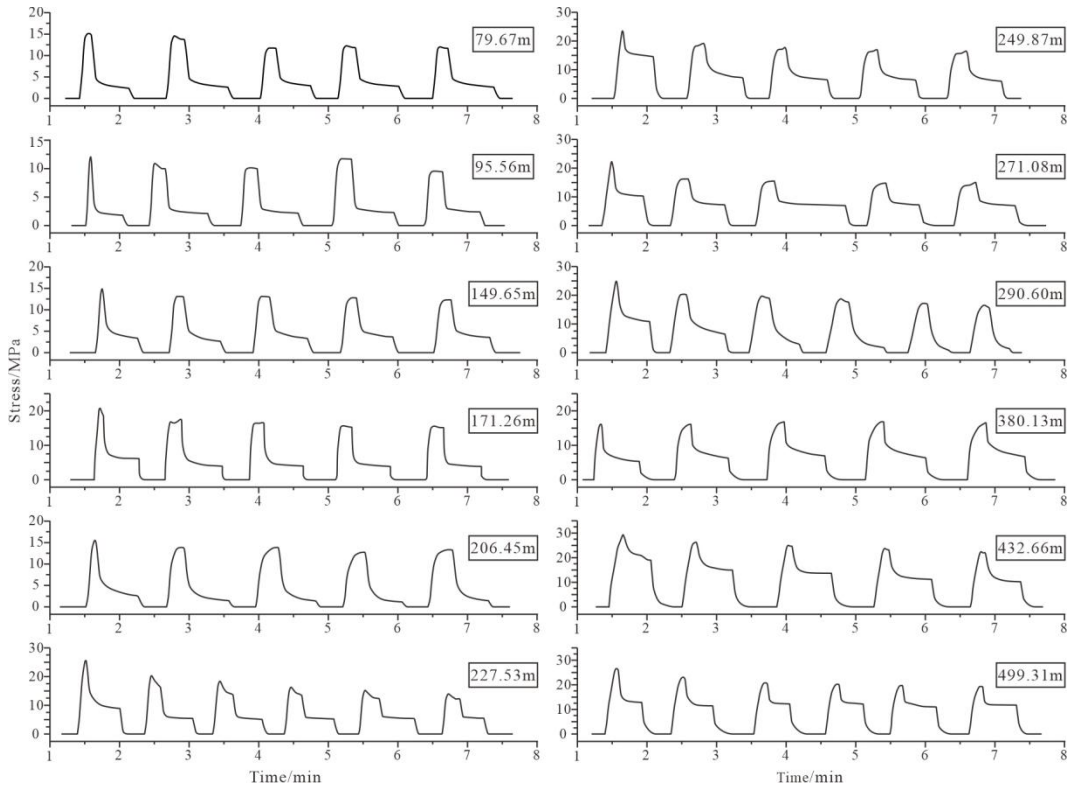



**Figure 4.** Curves of hydraulic fracturing in situ stress measurement.

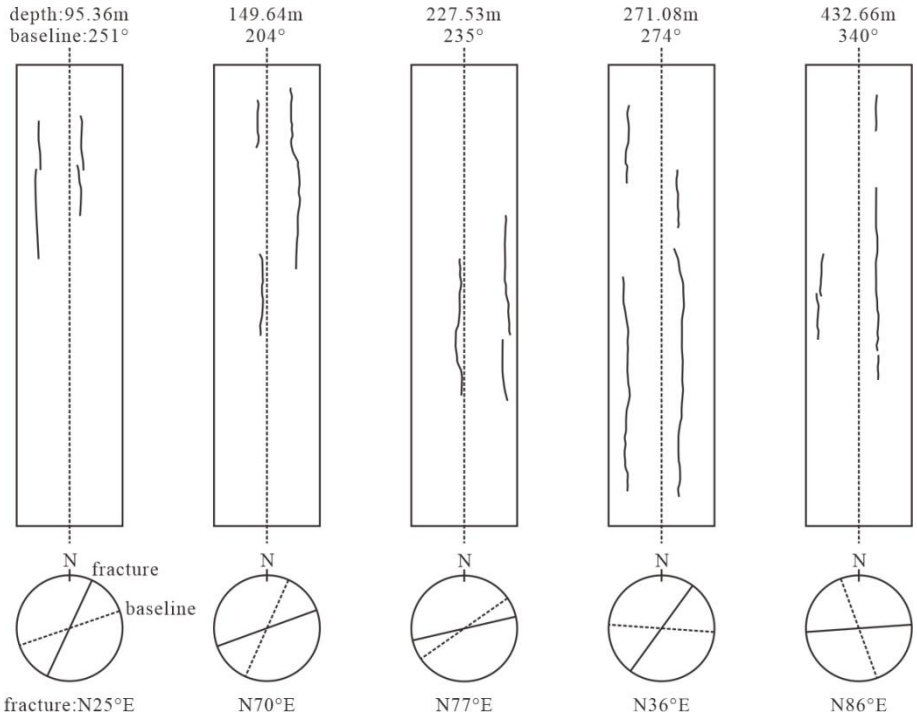



**Figure 5.** Impressions and orientations of hydraulic fractures.

**Table 2.** Summary and calculations of stress data based on the hydrofracturing method.

| No. | Depth (m) | Key Parameters of HF (MPa) | | | | | Stress (MPa) | | | $S_H$ Orientation |
|---|---|---|---|---|---|---|---|---|---|---|
| | | $P_H$ | $P_0$ | $P_b$ | $P_r$ | $P_s$ | $S_H$ | $S_h$ | $S_V$ | |
| 1 | 79.67 | 0.80 | 0.70 | 15.84 | 10.83 | 5.85 | 6.02 | 5.85 | 2.11 | |
| 2 | 95.56 | 0.96 | 0.86 | 13.13 | 8.86 | 4.88 | 4.92 | 4.88 | 2.53 | N 25° E |
| 3 | 149.65 | 1.50 | 1.40 | 16.34 | 11.53 | 7.54 | 9.69 | 7.54 | 3.97 | N 70° E |
| 4 | 171.26 | 1.71 | 1.61 | 22.45 | 14.84 | 8.85 | 10.10 | 8.85 | 4.54 | |
| 5 | 206.45 | 2.06 | 1.96 | 17.46 | 12.74 | 8.52 | 10.86 | 8.52 | 5.47 | |
| 6 | 227.53 | 2.28 | 2.18 | 27.68 | 14.39 | 9.19 | 11.00 | 9.19 | 6.03 | N 77° E |
| 7 | 249.87 | 2.50 | 2.40 | 26.06 | 16.75 | 14.48 | 24.29 | 14.48 | 6.62 | |
| 8 | 271.08 | 2.71 | 2.61 | 24.99 | 16.20 | 12.12 | 17.55 | 12.12 | 7.18 | N 36° E |
| 9 | 290.60 | 2.91 | 2.81 | 28.02 | 20.78 | 14.27 | 19.22 | 14.27 | 7.70 | |
| 10 | 380.13 | 3.80 | 3.70 | 19.89 | 16.98 | 15.14 | 24.74 | 15.14 | 10.07 | |
| 11 | 432.66 | 4.33 | 4.23 | 33.76 | 25.54 | 21.30 | 34.13 | 21.30 | 11.47 | N 86° E |
| 12 | 499.31 | 4.99 | 4.89 | 31.44 | 22.73 | 19.51 | 30.91 | 19.51 | 13.23 | |

Within the 500 m depth interval, the $S_H$ values range from 4.92 to 30.91 MPa, $S_h$ values range from 4.88 to 21.30 MPa, and $S_V$ values range from 2.11 to 13.23 MPa. The three-dimensional principal stress increases with depth, with fitting gradients of 0.0706 MPa/m, 0.0384 MPa/m, and 0.0265 MPa/m, respectively (Figure 6). The relationship among the three-dimensional principal stresses is $S_H > S_h > S_V$, indicating that the ground stress field is dominated by horizontal stress. The $S_H$ orientation is N 70°~86° E, with an average of N 78° E, which is consistent with the present tectonic stress field in North China. The orientation of the $S_H$ is NNE in a few intervals, possibly due to near-surface effects and local structural controls.

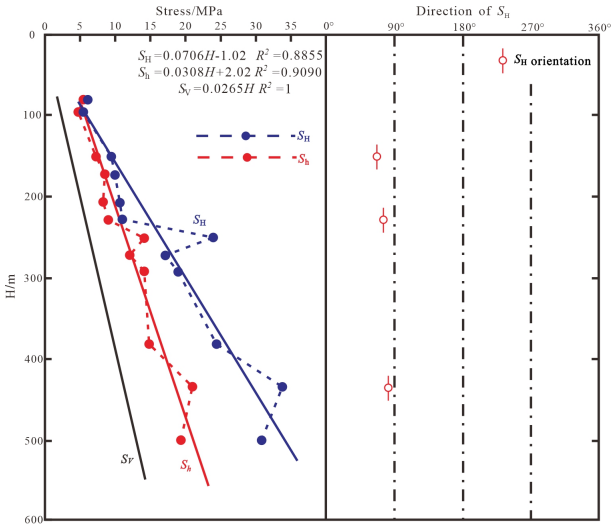



**Figure 6.** Trend of principal stress state of Zhangbei borehole with depth.

*4.2. Dynamic Adjustment Analysis of In Situ Stress Field*

The monitoring instrument at Zhangbei Station is installed at a depth of 104.5 m, with the four sets of probes oriented in the following orientations: NE 65° (P1), NW 335° (P2), NE 20° (P3), and NW 290° (P4). Data collection commenced on 4 November 2015 and has continued successfully, except for a period from 19 November 2017 to 23 May 2018 when data reception was interrupted due to equipment failure. Despite this interruption, the monitoring data have been largely continuous, effectively recording the dynamic adjustment process of the in situ stress field in the Zhangbei strong seismic region from November 2015 to October 2020 (Figure 7).

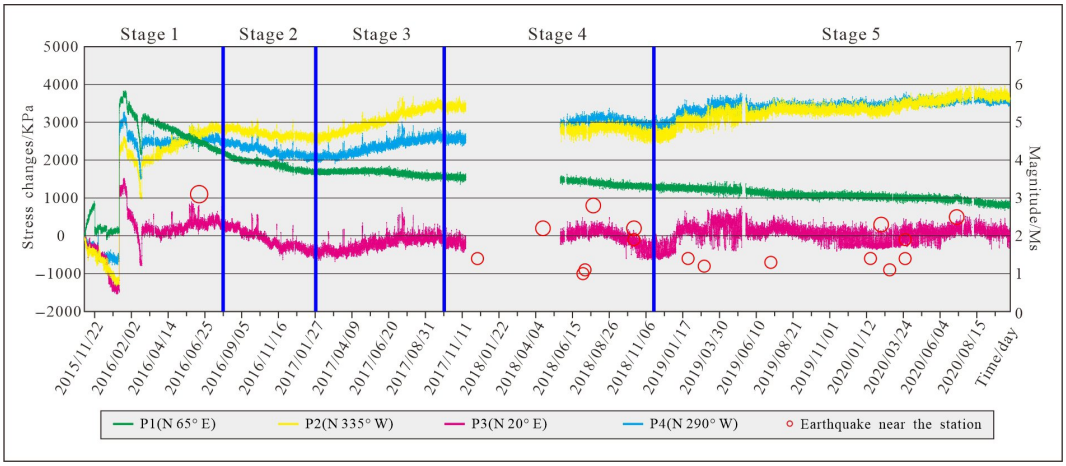



**Figure 7.** Curve of relative changes in in situ stress at the Zhangbei Station from October 2015 to October 2020.

The dynamic adjustment process of the in situ stress field from 4 November 2015 to 19 October 2020 can be divided into five stages: stage 1 (4 November 2015–31 July 2016), stage 2 (31 July 2016–28 January 2017), stage 3 (28 January 2017–26 September 2017), stage 4 (26 September 2017–7 December 2018), and stage 5 (7 December 2018–19 October 2020).

Due to the absence of measured data at the 104.5 m monitoring depth, initial values of $S_H$ and $S_h$ were based on data measured at 149.65 m. The reasons for taking the values are mainly based on the following three points. (1) Within the depth interval of 90–150 m, there is no lithological variation nor any major faults or intense tectonic disturbances, and horizontal principal stresses exhibit no significant abrupt changes with depth. (2) Direct application of in situ measured values also circumvents calculation errors induced by gradient fitting formulas. (3) Minor absolute deviations in the initial values only shift the baseline of stress time-series curves and exert no substantial influence on the dynamic evolution characteristics of in situ stress or the analysis of fault stability.

The relative changes in normal stress at the end of each stage were extracted, and the dynamic changes of the in situ stress field were analyzed using the aforementioned Formulas (1) and (2). The results are presented in Table 3.

**Table 3.** Dynamic adjustment results of the in situ stress field in the Zhangbei strong seismic region.

| Time | Component Variation (MPa) | | | | $S_H$ (MPa) | $S_h$ (MPa) | $S_H$ Orientation |
|---|---|---|---|---|---|---|---|
| | $\Delta\sigma_1$ | $\Delta\sigma_2$ | $\Delta\sigma_3$ | $\Delta\sigma_4$ | | | |
| Initial stage | 0 | 0 | 0 | 0 | 9.69 | 7.54 | N 70.0°~86.0° E |
| Stage 1 | −1.0228 | 1.1063 | −1.1339 | 0.1628 | 11.20–11.30 | 6.99–7.09 | N 69.4°~77.4° E |
| Stage 2 | −1.5078 | 0.5192 | −2.3390 | −0.5493 | 10.31–10.47 | 6.32–6.48 | N 66.1°~74.4° E |
| Stage 3 | −1.6932 | 1.6045 | −1.7278 | 0.0967 | 11.46–11.65 | 6.23–6.41 | N 65.7°~71.9° E |
| Stage 4 | −2.0071 | 0.7507 | −2.3350 | 0.2364 | 10.72–10.99 | 6.07–6.34 | N 61.4°~67.9° E |
| Stage 5 | −2.3657 | 1.6060 | −2.0454 | 0.9239 | 11.68–11.99 | 5.81–6.11 | N 60.3°~65.3° E |

Stage 1 (4 November 2015–31 July 2016) is the initial monitoring stage. This stage saw significant fluctuations in the monitoring curves due to contact coupling between the monitoring equipment and the borehole wall. This process lasted until 24 February 2016, after which the monitoring data gradually stabilized. Post-coupling, the stress value in the P1 orientation consistently decreased, while the P2 orientation showed an increasing trend. The P3 and P4 orientations saw slight increases over time. These observations suggest a weakening of the NEE compressional tectonic effect and a relative enhancement of the

NNW compressional tectonic effect in the Zhangbei strong seismic region, although overall compression remained predominantly NEE-oriented.

Starting from stage 2 (31 July 2016–28 January 2017), the monitoring value in the P1 orientation continued to decrease slightly, the P3 orientation remained stable with minor fluctuations, and the P2 and P4 orientations showed slight increases. These changes, in combination with the initial in situ stress field, indicate that the tectonic environment in the Zhangbei strong seismic region is primarily governed by NEE-trending compressional tectonic activity. This is consistent with the broader North China region. The overall tectonic environment showed continuous stress accumulation, with a slight enhancement in the NWW-trending compression effect. As of 19 October 2020, the $S_H$ value at the monitoring depth was between 11.68 and 11.99 MPa, the $S_h$ value ranged from 5.81 to 6.11 MPa, and the $S_H$ orientation was between N 60.3° and 65.3° E.

## 5. Probabilistic Analysis of Fault Stability

### *5.1. Simplified Fault Model*

This paper discusses the probability of slip instability of the main active faults in the Zhangbei strong seismic region. Based on the research results of the Hebei Earthquake Agency [18] and other scholars on fault structures in the Zhangbei strong seismic region, we collected information on the main faults and simplified the faults according to differences in strike, as shown in Figure 8 and Table 4.

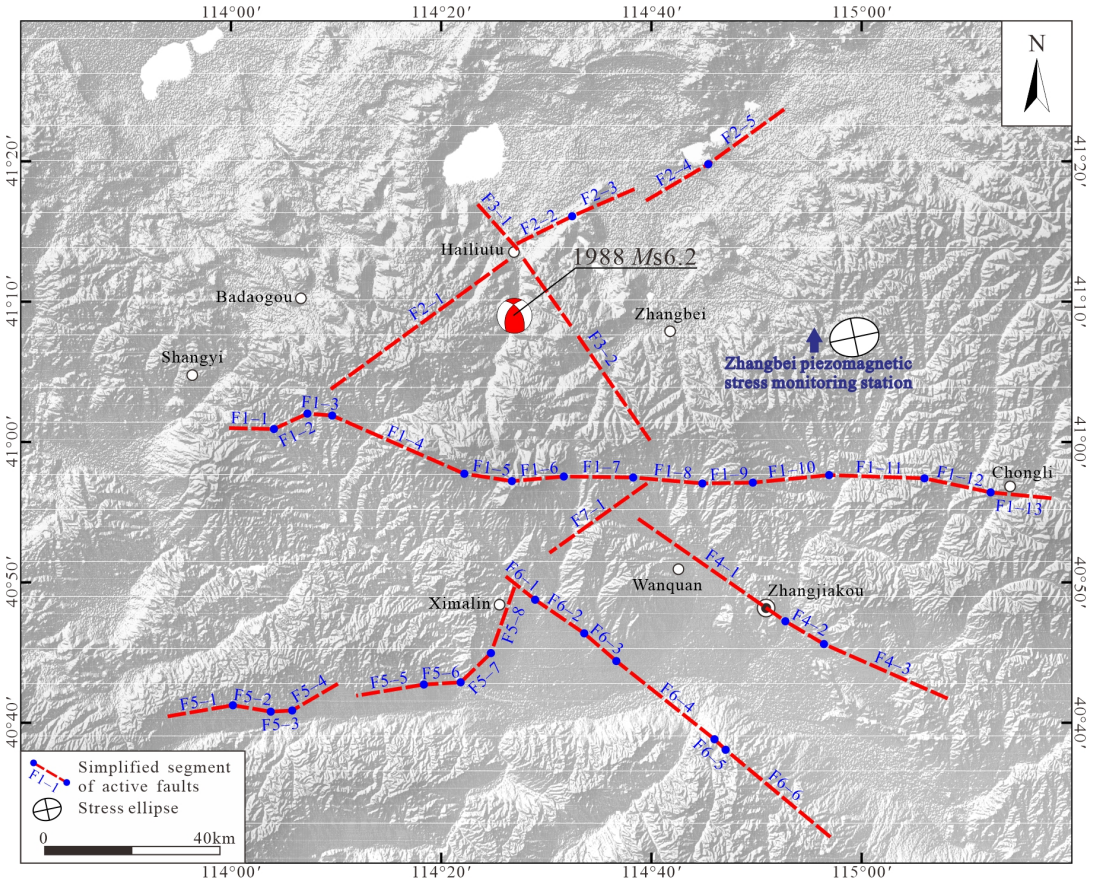



**Figure 8.** Simplified sectional characteristics of the main active faults in the Zhangbei strong seismic region.

**Table 4.** Results of fault occurrence and stability in Zhangbei strong seismic region.

| Fault | Section | Strike | Dip | Initial | Stage 1 | Stage 2 | Stage 3 | Stage 4 | Stage 5 |
|---|---|---|---|---|---|---|---|---|---|
| Shangyi–Pingquan fault (F1) | F1–1 | 271.2° ± 5° | 70° ± 10° | 0 | 14 | 23 | 51 | 52 | 85 |
| | F1–2 | 65.2° ± 5° | 70° ± 10° | 0 | 0 | 0 | 0 | 0 | 7 |
| | F1–3 | 274.5° ± 5° | 70° ± 10° | 0 | 19 | 31 | 59 | 53 | 85 |
| | F1–4 | 293.8° ± 5° | 70° ± 10° | 1 | 30 | 31 | 51 | 38 | 52 |
| | F1–5 | 278.8° ± 5° | 70° ± 10° | 0 | 24 | 35 | 60 | 54 | 80 |
| | F1–6 | 84.9° ± 5° | 70° ± 10° | 0 | 3 | 14 | 40 | 46 | 77 |
| | F1–7 | 270.8° ± 5° | 70° ± 10° | 0 | 11 | 22 | 51 | 54 | 83 |
| | F1–8 | 274.9° ± 5° | 70° ± 10° | 0 | 18 | 33 | 60 | 52 | 85 |
| | F1–9 | 89.1° ± 5° | 70° ± 10° | 0 | 10 | 19 | 51 | 48 | 83 |
| | F1–10 | 84.3° ± 5° | 70° ± 10° | 0 | 2 | 10 | 38 | 46 | 78 |
| | F1–11 | 272° ± 5° | 70° ± 10° | 0 | 13 | 29 | 54 | 52 | 84 |
| | F1–12 | 282° ± 5° | 70° ± 10° | 0 | 28 | 38 | 61 | 51 | 74 |
| | F1–13 | 275.5° ± 5° | 70° ± 10° | 0 | 19 | 30 | 59 | 54 | 82 |
| Daman–Qianheishatu fault (F2) | F2–1 | 53.9° ± 5° | 25° ± 10° | 43 | 47 | 26 | 37 | 13 | 12 |
| | F2–2 | 63.6° ± 5° | 25° ± 10° | 38 | 32 | 9 | 7 | 3 | 5 |
| | F2–3 | 66.5° ± 5° | 25° ± 10° | 39 | 25 | 7 | 7 | 6 | 12 |
| | F2–4 | 59.6° ± 5° | 25° ± 10° | 40 | 36 | 14 | 15 | 2 | 1 |
| | F2–5 | 54.2° ± 5° | 25° ± 10° | 42 | 45 | 25 | 34 | 13 | 8 |
| Miaodongying–Dayingtan fault (F3) | F3–1 | 318.5° ± 5° | 75° ± 10° | 20 | 38 | 33 | 40 | 30 | 40 |
| | F3–2 | 324.8° ± 5° | 75° ± 10° | 19 | 35 | 27 | 38 | 29 | 35 |
| | F3–3 | 325.5° ± 5° | 75° ± 10° | 22 | 34 | 27 | 35 | 26 | 33 |
| Zhangjiakou fault (F4) | F4–1 | 304.9° ± 5° | 60° ± 10° | 21 | 51 | 42 | 59 | 46 | 54 |
| | F4–2 | 300.6° ± 5° | 60° ± 10° | 18 | 48 | 46 | 60 | 52 | 62 |
| | F4–3 | 293.8° ± 5° | 60° ± 10° | 20 | 52 | 50 | 68 | 59 | 77 |
| The northern margin fault of Huaian Basin (F5) | F5–1 | 80.3° ± 5° | 65° ± 10° | 4 | 5 | 10 | 28 | 36 | 72 |
| | F5–2 | 279.6° ± 5° | 65° ± 10° | 8 | 35 | 41 | 67 | 61 | 87 |
| | F5–3 | 86.9° ± 5° | 65° ± 10° | 5 | 15 | 23 | 52 | 51 | 83 |
| | F5–4 | 59.7° ± 5° | 65° ± 10° | 6 | 11 | 2 | 5 | 0 | 0 |
| | F5–5 | 80.6° ± 5° | 65° ± 10° | 4 | 4 | 10 | 27 | 39 | 73 |
| | F5–6 | 86.6° ± 5° | 65° ± 10° | 5 | 13 | 22 | 49 | 53 | 87 |
| | F5–7 | 46° ± 5° | 65° ± 10° | 8 | 33 | 29 | 49 | 30 | 44 |
| | F5–8 | 19.7° ± 5° | 65° ± 10° | 12 | 37 | 41 | 63 | 58 | 87 |
| Ximalin fault (F6) | F6–1 | 308.6° ± 5° | 75° ± 10° | 11 | 34 | 30 | 43 | 29 | 39 |
| | F6–2 | 304.4° ± 5° | 75° ± 10° | 11 | 36 | 38 | 49 | 36 | 47 |
| | F6–3 | 310.8° ± 5° | 75° ± 10° | 9 | 32 | 27 | 38 | 28 | 37 |
| | F6–4 | 308.6° ± 5° | 75° ± 10° | 10 | 34 | 29 | 44 | 29 | 39 |
| | F6–5 | 313.3° ± 5° | 75° ± 10° | 10 | 30 | 23 | 36 | 24 | 31 |
| | F6–6 | 309.8° ± 5° | 75° ± 10° | 11 | 34 | 29 | 42 | 31 | 35 |
| Xinkaikou fault (F7) | F7–1 | 54.5° ± 5° | 65° ± 10° | 15 | 27 | 13 | 22 | 5 | 6 |

### 5.2. Parameter Uncertainty

In this study, using FSP software, we considered uncertainties in several parameters when analyzing the instability probability of fault activity in the Zhangbei strong seismic region. These parameters include the $S_H$ value, $S_h$ value, $S_H$ orientation, pore water pressure, fault strike, fault dip angle, and critical friction coefficient. Table 3 shows that the $S_H$ value, $S_h$ value, and $S_H$ orientation in the initial stage and subsequent five in situ stress monitoring stages in the Zhangbei strong seismic region fall within certain ranges, indicating inherent uncertainties. Table 4 presents the simplified segmentation of faults, which inevitably introduces errors in fault strike. To fully account for the impact of uncertainties in fault strike and dip on the initial stability state of faults, we assigned

error values of ±5° for strike and ±10° for dip based on relevant reference materials. The groundwater level in the strong seismic region is dynamically variable, leading to uncertainty in pore water pressure. According to the monitoring results at Zhangbei Station from 2015 to 2020, the groundwater level near the station is 32.2 ± 0.4 m. It should be noted that all stress parameters adopted for fault stability calculation in FSP software are effective stresses.

For the selection of critical friction coefficients for major active faults, the empirical friction coefficient (μ) of 0.6 is generally used as the critical value for judging fault instability [29–32]. However, studies have shown that the μ value reflected by the actual crust during the stress accumulation process may be lower than 0.6. For instance, the μ value of the San Andreas fault system is 0.18–0.26 [33,34]. Townend [32] and Zoback [35] provided the ratio of measured shear stress to normal stress on the fracture surface at multiple research sites, indicating that about 10–20% of the data can approach or exceed the value limited by μ = 0.6, but most are lower. Zoback [36] suggested that the criterion for reverse fault instability might be that the maximum effective principal stress equals approximately 2.2 times the vertical effective principal stress (μ is about 0.4), whereas for a normal fault it might be that the minimum effective principal stress equals roughly 0.6 times the vertical effective principal stress (μ is about 0.2). Feng [37] studied the activity of the Tanlu Fault Zone and adjacent areas using in situ stress measurement data and found that the calculated apparent friction coefficients of the fault in the Changli area were generally low (0.21–0.45). Considering existing research results and the nature of fault activity in the Tangshan strong seismic region, we adopted a critical friction coefficient of 0.4 ± 0.2 for analyzing the probability of fault sliding instability in the Zhangbei strong seismic region.

Using the Shangyi–Pingquan fault F1–1 segment as an example, the FSP program conducted random sampling of key parameters within their error ranges according to the Monte Carlo method and re-determined the probability distribution characteristics of each expected value, as shown in Figure 9.

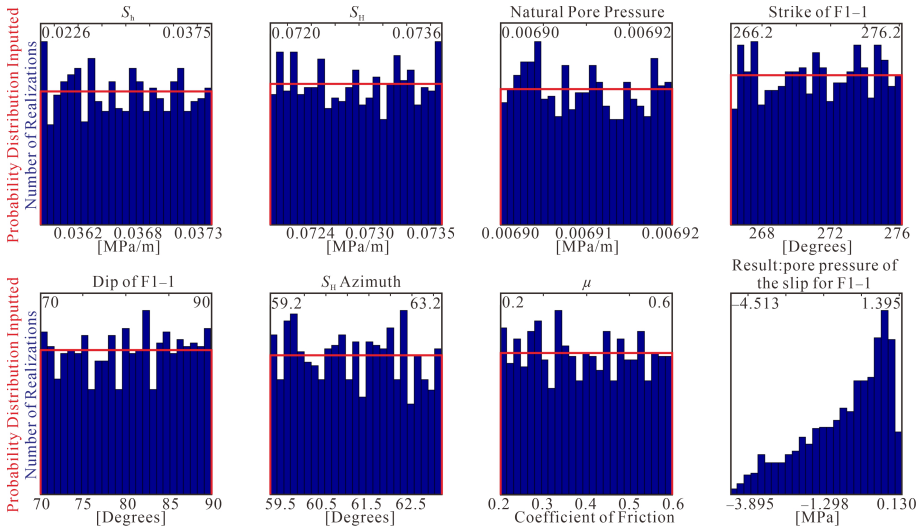



**Figure 9.** Probability distribution of in situ stress field and F1–1 fault attribute parameters in Zhangbei strong seismic region.

### *5.3. Calculation Results of Fracture Sliding Instability Probability*

This paper discusses the probability of slip instability of the main active faults in the Zhangbei strong seismic region based on the research results of the Hebei Provincial Seismological Bureau [18] and other scholars on fault structures in the Zhangbei.

The slip instability probability calculations for the main faults in the Zhangbei strong seismic region are presented in Table 4 and Figure 10. Based on these results and the existing earthquake distribution in the strong seismic region, we discuss the fault activity at each stage.

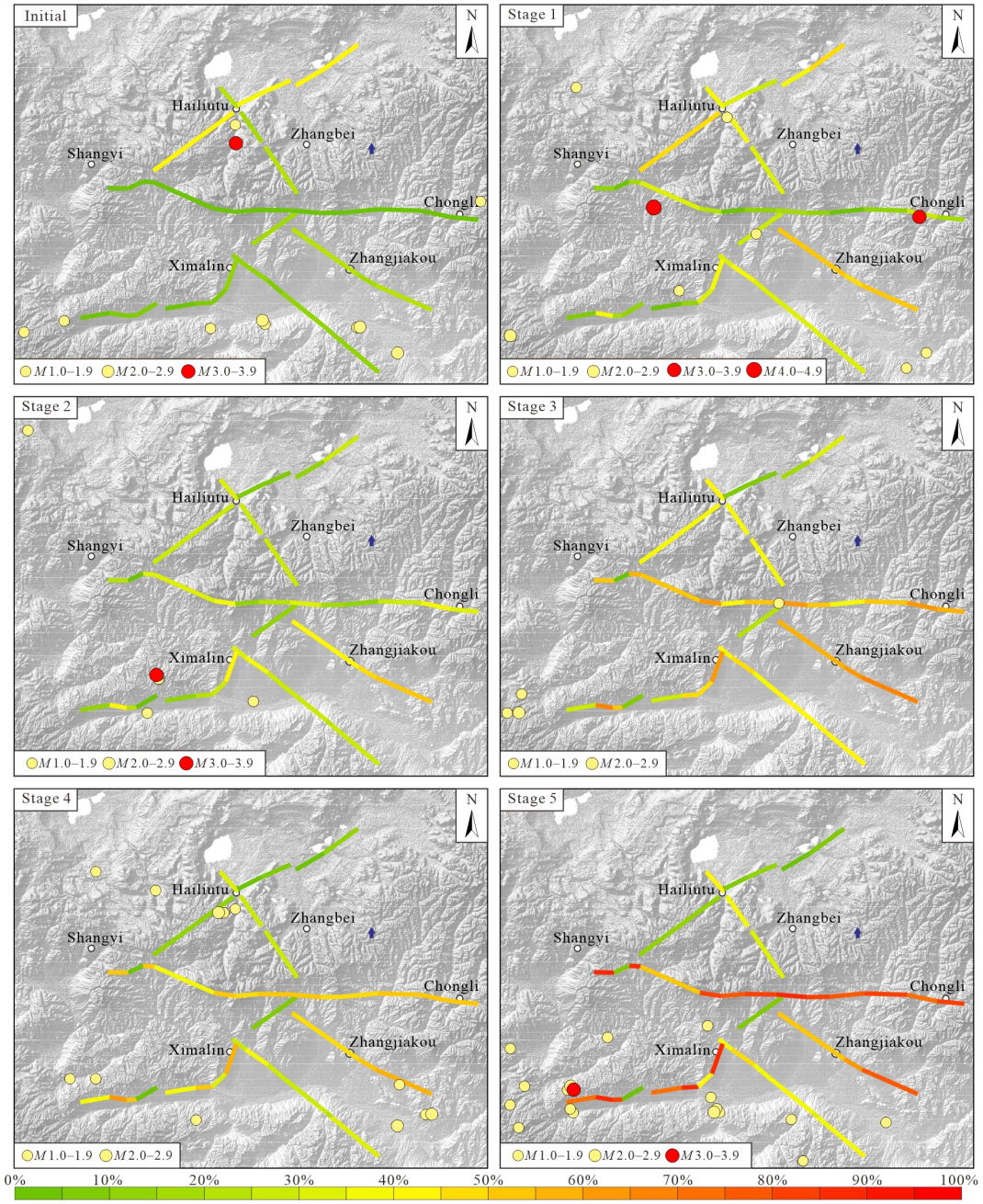



**Figure 10.** Results of probability analysis of slip instability of main faults in the Zhangbei strong seismic region.

In the initial stage, under the NEE in situ stress field, the NE-trending faults in the strong seismic region are the most active, followed by the NW-trending and NNE-trending faults, while those near EW-trending faults are the least active. The stress accumulation level of faults in the northern part of the strong seismic region is higher than in the southern part. The Daman–Qianheishatu fault shows the highest stress accumulation with FSP values of 38–43%, indicating a higher potential for sliding instability. The Shangyi–Pingquan fault and the northern margin fault of the Huaian Basin have the lowest stress

accumulation levels, with FSP values mainly below 10%, indicating a lower potential for sliding instability. Earthquake statistics from October 2014 to October 2015 indicate low seismic activity, with predominantly small earthquakes (M < 3.0) scattered in the southern part of the strong seismic region and the intersection of the Daman–Qianheishatu Fault and the Miaodongying–Dayingtan Fault. A notable event was the *Ms* 3.1 earthquake on 12 June 2015 at this intersection.

From stage 1, affected by the continuous adjustment of the regional tectonic stress field, the stress accumulation levels of NWW-trending, NEE-trending, and near-EW-trending faults in the strong seismic region increased gradually, while the NE-trending faults experienced a relative decrease. By the end of stage 5, the highest stress accumulation levels were observed in the Shangyi–Pingquan fault, Zhangjiakou fault, and the northern margin fault of the Huaian Basin, with FSP values ranging from 44 to 87%. The Miaodongying–Dayingtan fault and the Ximalin fault followed, with FSP values between 31 and 47%. The lowest stress accumulation levels were in the Daman–Qianheishatu fault and the Xinkaikou fault, with FSP values mainly between 1 and 12%. The stress accumulation in the southern part of the strong seismic region was stronger than in the northern part, with the Shangyi–Pingquan fault serving as a boundary.

The seismic activity in the strong seismic region is also consistent with the calculation results. Since 11 October 2015, the strong seismic region has continued to experience small earthquakes and micro-earthquakes, indicating ongoing stress accumulation. However, the earthquake distribution area has gradually shifted from the northern part to the southern part of the strong seismic region, with causative faults predominantly being NWW, NEE, and near-EW faults. Significant events include an *Ms* 3.1 and *Ms* 4.0 earthquake on 18 March 2016 and 23 June 2016, respectively, in the eastern and western sections of the Shangyi–Pingquan Fault. On 2 January 2017, an *Ms* 3.6 earthquake occurred in the middle section of the northern margin fault of the Huaian Basin, and on 19 May 2020 an *Ms* 3.3 earthquake occurred at the southwestern end of the same fault.

## 6. Discussion

### *6.1. The Current In Situ Stress Field in the Zhangbei Seismic Region*

Existing results from GPS observations, fault deformation studies, and numerical simulations of tectonic motion in North China consistently indicate that the present-day stress field is jointly controlled by surrounding plate interactions and relative motions among intracontinental blocks [38–40]. Affected by the northward indentation of the Indian Plate, the western boundary of the North China Block is predominantly subjected to NEE-trending compressional tectonism. Meanwhile, the westward subduction of the Pacific Plate impedes the eastward movement of the North China Block. Under the long-term action of the above two tectonic background fields, the crustal stress field of the North China Block is generally characterized by NEE-trending compressional tectonism. Concurrently, the intensity of this compression dynamically adjusts in accordance with the magnitude of the relative motions between the Indian Plate, the Pacific Plate, and the Eurasian Plate [41,42]. Owing to the widespread rigid basement in the Yanshan region of northern North China, intracontinental deformation is obstructed at the piedmont of the Yanshan Mountains, forming an overall tectonic regime dominated by sinistral strike–slip and compression at the northern margin of the North China Plain. This also represents the primary tectonic characteristic of the Zhangjiakou–Bohai Fault Zone [43].

The Zhangbei strong seismic region is located on the northwestern margin of the North China Block at the junction between the Zhangjiakou–Bohai tectonic belt (the Zhang–Bo belt) and the Shanxi graben system. This tectonic setting implies that the in situ stress field of the Zhangbei strong seismic region is governed not only by far-field plate forcing but

also by the combined effects of the segmented activity of the Zhang–Bo belt and the Shanxi graben system. The Shanxi Graben System is composed of five fault-depressed basins in a south to north sequence, the Yuncheng, Linfen, Taiyuan, Xinding, and Datong Basins, exhibiting an overall obliquely stretched "S" shape. The northeastern end of the Datong Fault-Depressed Basin extends in an NEE-trending direction into the Yuxian–Huailai Basin and connects with the Zhangjiakou–Bohai Fault Zone. Research results of focal mechanisms demonstrate that the tectonic deformation pattern of the Shanxi Graben System generally features an extensional stress field in its central part and strike–slip stress fields at its southern and northern termini [39,44–46]. Meanwhile, focal mechanism solutions in the Zhangbei strong seismic region are dominated by the strike–slip type [47]. Accordingly, it can be inferred that the local in situ stress field in the Zhangbei strong seismic region is predominantly controlled by the Zhangjiakou–Bohai Fault Zone.

Numerous studies involving focal mechanism solutions, numerical simulations, and GPS observations have validated that the Tohoku–Oki 3.11 M9.0 earthquake induced the dynamic adjustment of the tectonic environment in eastern China. Meanwhile, relevant research indicates that tectonic activity of the Zhangjiakou–Bohai Fault Zone exhibited a gradually declining trend after this earthquake, and its Zhangjiakou segment presents relatively high AMR values [48], signifying a persistent state of stress accumulation. The stress magnitudes of two monitoring components, namely, P2 (N 335° W) and P4 (N 290° W), at the Zhangbei In Situ Stress Monitoring Station have maintained a steady, slow increase, which is consistent with the current kinematic state of the Zhangjiakou–Bohai Fault Zone. Although measured in situ stress data before the Tohoku–Oki 3.11 M9.0 earthquake are unavailable for comparative analysis in the Zhangbei strong seismic region, the sustained slow growth in the magnitude of the $S_H$ reflected by the monitoring data demonstrates that the seismic region is currently in a stage of continuous stress accumulation.

Measured in situ stress data from the Zhangbei strong seismic region show that the present $S_H$ orientation in the shallow subsurface is NEE-trending, which is consistent with the present in situ stress field in North China and the analytical results of deep focal mechanism solutions in the seismic region. The magnitude relationship of the three principal stresses follows the order of $S_H > S_h > S_V$, and it is inconsistent with the nature of fault activity in the strong earthquake zone. This discrepancy arises because the regional normal faults are relics of paleo-extensional tectonics, whereas the measured in situ stress reflects the current tectonic dynamic setting.

### 6.2. Coupling Relationship Between Shallow and Deep In Situ Stress Fields

The regional in situ stress field is governed by tectonic movements, and stress magnitudes increase regularly with burial depth; meanwhile, both the magnitude and orientation of in situ stress exhibit favorable continuity between the shallow subsurface and deep strata. Constrained by the testing depth and the installation depth of monitoring instruments, only measured in situ stress data within several hundred meters below the ground surface in the Zhangbei strong seismic region can be obtained. Such measured data can accurately define core parameters, including the orientation of regional principal stresses and the stress state; however, the direct measurement of in situ stress at depths of several to more than ten kilometers is currently unachievable due to technical limitations.

Dynamic adjustment of the shallow subsurface in situ stress field is correlated with deep tectonic activities. Liao et al. [49] conducted in situ stress measurements and post-earthquake remeasurements at the same sites before and after the *Ms* 8.1 Kunlun Mountains earthquake, capturing changes in shallow subsurface in situ stress triggered by the earthquake. The remeasurement results indicated that the $S_H$ at the identical depth was 12 MPa before the earthquake but dropped sharply to 3–4 MPa after the earthquake. Guo et al. [50]

also obtained evidence that the earthquake altered the regional in situ stress field through hydraulic fracturing in situ stress measurements carried out in the Guangyuan–Qingchuan section of the Longmenshan Fault Zone before and after the *Ms* 8.0 Wenchuan earthquake. Before the Wenchuan earthquake, the $S_H$ within the borehole depth range of 350–420 m was measured as 21–22 MPa; one week after the earthquake, remeasurements at the same depth interval showed that the $S_H$ decreased significantly to approximately 15 MPa.

The $S_H$ orientation obtained in this study corresponds well with analytical results of deep focal mechanism solutions. Based on shallow measured data, scientific evaluation was conducted of the stability of major faults by combining the Mohr–Coulomb Criterion and Byerlee's Law. Although the research findings cannot achieve an accurate quantitative determination of deep fault stability, they can effectively reveal the tectonic stress environment and macroscopic stability trends of deep faults, thus possessing certain scientific merit and engineering guiding significance.

Admittedly, shallow subsurface testing data inevitably present discrepancies and errors due to the influences of local topography and tectonic conditions. Meanwhile, the deep tectonic environment is complex, characterized by variable fault occurrence, petrophysical and mechanical properties of rocks, and pore pressure. The activity of deep faults is not restricted to brittle failure but also includes diverse types, such as creep and viscoelastic relaxation. Therefore, the analysis of the shallow crustal in situ stress field and deep fault stability in the Zhangbei strong seismic region based on shallow subsurface measured data has certain limitations. To acquire a more comprehensive understanding of the shallow crustal in situ stress field characteristics and fault stability in the Zhangbei strong seismic region, more measured in situ stress data and research findings on deep tectonic environments should be collected, and deep in situ stress monitoring should be strengthened. In addition, further research is required on how to better analyze deep stress states and the transformation relationship between shallow and deep in situ stress regimes based on shallow in situ stress measurement results.

### *6.3. Contribution of Parameters to Fault Slip Potential of Zhangbei Strong Seismic Region*

The analysis of fault stability using FSP software is mainly based on the Mohr–Coulomb Criterion and Byerlee's Law. Thus, the core criterion for fault stability is still whether the shear stress accumulated on the fault plane exceeds its effective shear strength.

Seven parameters, namely the $S_H$ value, $S_h$ value, $S_H$ orientation, pore water pressure, fault strike, fault dip angle, and critical friction coefficient, were selected for the fault stability analysis of the Zhangbei strong seismic region, and the errors of all computational parameters were considered. All seven parameters can directly affect the shear stress or effective shear strength on the fault plane.

The calculation results of fault slip potential respond significantly to the dynamic changes in $S_H$ value, $S_h$ value, and $S_H$ orientation. However, because the error ranges of the above three parameters and pore water pressure are relatively small, their errors exert no obvious influence on the calculation results. In contrast, the errors of the critical friction coefficient and the fault dip angle have the greatest impacts on the calculation results, while fault strike has a relatively minor effect.

It should be noted that a relatively wide range is adopted for the critical friction coefficient mainly to account for the complexity of actual fault conditions. Compared with setting the critical friction coefficient as a fixed value, the calculated results of fault stability in the strong earthquake zone increase significantly, but no substantial changes are observed.

## 7. Conclusions

This paper evaluates the dynamic adjustment of the in situ stress field and the stability of main faults in the Zhangbei strong seismic region utilizing in situ stress monitoring data from November 2015 to October 2020. We present findings on the regional stress behavior and fault stability underpinning potential risks and seismic activities within the zone.

1. Trends in the in situ stress field:

Since November 2015, the stress field has been predominantly governed by NEE-trending compressional tectonic actions. Compared with October 2015, recent data indicate a slight rise in $S_H$ values and a corresponding decrease in $S_h$ values, with the stress field remaining predominantly NEE-trending. As of October 19, 2020, at the monitoring depth of 104.5 m, the $S_H$ value ranged from 11.68 to 11.99 MPa, the $S_h$ value from 5.81 to 6.11 MPa, and the $S_H$ orientation from N 60.3° E to N 65.3° E.

2. Fault stability analysis:

In the initial stage, NE-trending faults exhibited the highest stress accumulation levels, with NW-trending faults showing lower levels and near-EW-trending faults the lowest. Starting from stage 1, the $S_H$ orientation has undergone a slight adjustment, and the $S_H$ value is continuously and slowly increasing. This shift contributed to increased stress accumulation in near-EW-trending and NW-trending faults, whereas NE-trending faults saw a reduction. By October 2020, near-EW-trending faults displayed the highest stress accumulation, followed by NW-trending faults, with NE-trending faults showing the least accumulation.

3. Seismic activity and fault risk:

The continuous slight northward shift in the in situ stress field's orientation increased stress accumulation in the southern part of the strong seismic region, making it more seismically active than the north. Notably, earthquakes with magnitudes $\geq 3.0$ were predominantly located in the southern region. This spatial distribution of seismic activity highlights a greater risk of fault instability in the southern part of the zone compared to the north. The data indicate that the area remains in a phase of continuous stress accumulation, raising the potential for medium to strong earthquakes in the future. It is necessary to further strengthen the monitoring of the in situ stress field and fault stability in the Zhangbei strong seismic region.

This study provides vital insights into the tectonic dynamics of the Zhangbei strong seismic region and underscores the importance of continuous monitoring to mitigate potential earthquake risks.

Conducting shallow in situ stress measurements and real-time monitoring in a strong seismic region to obtain the initial stress field and its temporal variations in the seismogenic fault and adjacent areas and, on this basis, evaluating the time-dependent probability of fault slipping instability along the major seismogenic faults using the Mohr–Coulomb criterion can provide effective support for forecasting and assessing seismic activity hazards in strong seismic regions.

**Author Contributions:** Conceptualization, J.M. and Y.F.; methodology, Y.F. and C.F.; software, C.F.; validation, J.M., Y.F. and C.F.; formal analysis, Y.F.; investigation, B.Q., P.Z. and C.F.; resources, C.T.; data curation, J.M. and Y.F.; writing—original draft preparation, J.M. and Y.F.; writing—review and editing, J.M. and C.F.; visualization, Y.F.; supervision, C.F. and C.T.; project administration, P.Z. and C.F.; funding acquisition, C.F. All authors have read and agreed to the published version of the manuscript.

**Funding:** This research was funded by the project of the China Geological Survey, grant numbers DD20230540, DD20190317 and DD202606201408.

**Data Availability Statement:** The data presented in this study are available on request from the corresponding author (the raw monitoring data is of enormous volume and requires professional interpretation, thus precluding the direct provision of the original dataset).

**Acknowledgments:** The authors would like to thank Xiaodong Ma and Shihuai Zhang (University of Science and Technology of China) for providing the FSP v.1.0 software package.

**Conflicts of Interest:** The authors declare no conflicts of interest.

## References

1. Ohnaka, M. Nonuniformity of the constitutive law parameters for shear rupture and quasistatic nucleation to dynamic rupture: A physical model of earthquake generation processes. *Proc. Natl. Acad. Sci. USA* **1996**, *93*, 3795–3802. [CrossRef]
2. Tan, C.X.; Zhang, P.; Lu, S.L.; Zhu, J.Z.; Feng, C.J.; Qin, X.H.; Meng, J. Significance and Role of In-Situ Crustal Stress Measuring and Real-time Monitoring in earthquake Prediction Research. *J. Geomech.* **2019**, *25*, 866–876. [CrossRef]
3. An, Q.M.; Sun, S.Z.; Liu, Y.Z. The inversion of tectonic stress field in North China from actual stress measurements. *N. China Earthq. Sci.* **1985**, *3*, 28–39.
4. Liang, H.Q.; Liu, J.Z.; Liu, Q.X. The relationship between present state of stress in part of active faults plane and their unsteady form in Southwest China. *Earthq. Res. China* **1993**, *9*, 48–55.
5. Feng, C.J.; Zhang, P.; Sun, W.F.; Qin, X.H.; Chen, Q.C.; Tan, C.X. A discussion on the impact of Japan Mw9.0 earthquake on the main active fault zone in north-and northeast-China continent and the seismic risk. *Earth Sci. Front.* **2013**, *20*, 123–140.
6. Fan, Y.L.; Tan, C.X.; Zhang, P.; Sun, M.Q.; Qi, B.S.; Feng, C.J.; Meng, J.; Wang, H.Q. A Study of current in-situ stress state and its influence on tectonic stability in the Xiongan New Area. *Acta Geosci. Sin.* **2020**, *41*, 481–491.
7. Tanaka, Y.; Fujimori, K.; Otsuka, S. In-Situ Stress Measurement and Prediction of Great Earthquake. *Earthquake* **1998**, *50*, 201–208.
8. Townend, J.; Zoback, M.D. Regional Tectonic Stress Near the San Andreas Fault in Central and Southern California. *Geophys. Res. Lett.* **2004**, *31*, L15S11. [CrossRef]
9. Tan, C.X.; Zhang, P.; Feng, C.J.; Qin, X.H.; Sun, W.F.; Chen, Q.C.; Wu, M.L. An Approach on Deep Borehole Crustal Stress Measuring and Real-Time Monitoring and Its Application in Seismogeology Research in Capital Beijing Region. *Acta Geol. Sin.* **2014**, *88*, 1436–1452.
10. Feng, C.J.; Zhang, P.; Sun, W.F.; Tan, C.X. The Application of in Situ Stress Measuring and Real-time Monitoring Results to Analyzing the Fault Activity Hazard at Ming Tombs Borehole in Changping District, Beijing. *Acta Geosci. Sin.* **2014**, *35*, 345–354. [CrossRef]
11. Qiu, J.; Wu, M.L.; Fan, T.Y.; Zhang, C.Y.; Li, R.; Chen, L.Z. Comparative Analysis of In-Situ Stress in the Southwestern Segment of Longmenshan Fault Zone before and after Lushan Earthquake. *Acta Geol. Sin.* **2017**, *91*, 969–978.
12. Walsh, R.; Zoback, M.D.; Pais, D.; Weingarten, M.; Tyrrell, T. *FSP1.0: A Program for Probabilistic Estimation of Fault Slip Potential Resulting form Fluid Injection*; Stanford Center for Induced and Triggered Seismicity (SCITS): Palo Alto, CA, USA, 2016.
13. Fu, Z.X.; Liu, J.; Liu, G.P. On the long-term seismic hazard analysis in the Zhangjiakou-Penglai seismotectonic zone, China. *Tectonophysics* **2004**, *390*, 75–83. [CrossRef]
14. Ju, W.; Sun, W.F.; Ma, X.J.; Jiang, H. Tectonic stress accumulation in Bohai-Zhangjiakou Seismotectonic zone based on 3D visco-elastic modelling. *J. Earth Syst. Sci.* **2016**, *125*, 1021–1031.
15. Lai, X.L.; Li, S.L.; Zhang, X.K.; Diao, G.L. 3-D structural feature in Zhangbei earthquake region. *Earth Sci. Front.* **2002**, *9*, 383–388.
16. Yang, Z.X.; Chen, Y.T.; Zhang, H.Z. Relocation and seismogenic structure of the 1998 Zhangbei-Shangyi earthquake sequence. *Acta Seismol. Sin.* **2002**, *15*, 383–394. [CrossRef]
17. Xie, J.; Zeng, X.F.; Chen, W.W.; Zhan, Z.W. Comparison of ground truth location of earthquake from InSAR and from ambient seismic noise: A case study of the 1998 Zhangbei earthquake. *Earthq. Sci.* **2011**, *24*, 239–247. [CrossRef]
18. Peng, Y.Q.; Meng, L.P. *Seismic Characteristics in Hebei*; Hebei People's Publishing House: Shijiazhuang, China, 2017; pp. 1–324.
19. Peng, Y.Q.; Sun, X.Y.; Zhan, Y.; Zhao, L.Q.; Liu, X.H.; Ran, Z.J.; Wang, L.S. 3D deep electrical structure and seismogenic environment in Zhangbei earthquake region. *Chin. J. Geophys.* **2022**, *65*, 3464–3480.
20. Amadei, B.; Stephansson, O. *Rock Stress and Its Measurement*; Chapman & Hall: London, UK, 1997.
21. Tan, C.X.; Sun, Y.; Wang, L.J. Some problems of in-situ crustal stress measurements. *J. Geomech.* **2003**, *9*, 275–280+260.
22. Tan, C.X.; Sun, W.F.; Sun, Y.; Wang, L.J. A consideration on in-situ crustal stress measuring and its underground engineering application. *Acta Geol. Sin.* **2006**, *80*, 1627–1632.
23. Wang, C.H.; Song, C.K.; Guo, Q.L.; Zhang, Y.S.; Ding, J.M. Stress build-up in the shallow crust before the Lushan Earthquake based on the in-situ stress measurements. *Chin. J. Geophys.* **2014**, *57*, 102–114.
24. Kang, H.P.; Yi, B.D.; Gao, F.Q.; Lv, W.H. Database and characteristics of underground in-situ stress distribution in Chinese coal mines. *J. China Coal Soc.* **2019**, *44*, 23–33.

25. Stacey, F.D.; Johnston, M.J.S. Theory of the piezomagnetic effect in titanomagnetite-bearing rocks. *Pure Appl. Geophys.* **1972**, *97*, 146–155. [CrossRef]
26. Carmichael, R.S. Depth calculation of piezomagnetic effect for earthquake prediction. *Earth Planet. Sci. Lett.* **1977**, *36*, 309–316. [CrossRef]
27. Ryu, J.; Priya, S.; Uchino, K.; Kim, H.E. Magnetoelectric effect in composites of magnetostrictive and piezoelectric materials. *J. Electroceram.* **2002**, *8*, 107–119. [CrossRef]
28. Li, T.L.; Yin, S.Y.; Li, T.J. *Elastic-Plastic Mechanics*; China University of Geosciences Press: Wuhan, China, 2016; pp. 1–308.
29. Byerlee, J.D. Friction of rocks. In *Rock Friction and Earthquake Prediction*; Byerlee, J.D., Wyss, M., Eds.; Birkhäuser: Basel, Switzerland, 1978; pp. 615–626.
30. Jamison, D.; Cook, N.G.W. Note on measured values for the state of stress in the earth's crust. *J. Geophysical. Res.* **1980**, *85*, 1833–1838. [CrossRef]
31. Norman, H.S. Rate-and state-dependent friction of intact rock and gouge. *J. Geophys. Res.* **1999**, *104*, 17847–17855.
32. Townend, J.; Zoback, M.D. How Faulting Keeps the Crust Strong. *Geology* **2000**, *28*, 399–402. [CrossRef]
33. Hickman, S.; Zoback, M.D. Stress orientations and magnitudes in the SAFOD pilot hole. *Geophys. Res. Lett.* **2004**, *31*, L15S12. [CrossRef]
34. Carpenter, B.M.; Marone, C.; Saffer, D.M. Weakness of the San Andreas fault revealed by samples from the active fault zone. *Nat. Geosci. Lett.* **2011**, *4*, 251–254. [CrossRef]
35. Zoback, M.D.; Zoback, M.L.; Van, S.M. New evidence on the state of stress of the San Andreas fault system. *Science* **1987**, *238*, 1105–1111. [CrossRef] [PubMed]
36. Zoback, M.D. *Reservoir Geomechanics*; Cambridge University Press: Cambridge, UK, 2007; pp. 123–139.
37. Feng, C.J.; Zhang, P.; Meng, J.; Qi, B.S.; Qin, X.H.; Niu, L.L.; Sun, D.S.; Sun, W.F.; Tan, C.X.; Chen, Q. In Situ Stress Measurement at Deep Boreholes along the Tanlu Fault Zone and Its Seismological and Geological Significance. *Prog. Geophys.* **2017**, *32*, 946–967.
38. Liu, X.; Ma, J.; Fu, R.S.; Yang, G.H.; Shao, Z.G.; Zhang, Z.J. Primary study on the dynamics of the present-day crustal motion in North China Region. *Chin. J. Geophys.* **2010**, *53*, 1418–1427.
39. Yang, Y.Y.; Li, Q.; Gu, Y.C. Analysis of surface vertical load deformation in the North China Plain from 2002 to 2023 using GRACE and GPS. *Sci. Surv. Mapp.* **2024**, *49*, 9–21.
40. Zhang, Z.F.; Zhang, H.; Guo, Y.C.; Shi, Y.L. Crustal deformation in North China based on GNSS strain rates. *Chin. J. Geophys.* **2026**, *69*, 113–126.
41. Zhao, B.; Zhang, C.H.; Wang, D.Z.; Huang, Y.; Tan, K.; Du, R.; Liu, J. Contemporary kinematics of the Ordos block, North China and its adjacent rift systems constrained by dense GPS observations. *Asian Earth Sci.* **2017**, *135*, 257–267. [CrossRef]
42. Wang, M.; Shen, Z.K. Present-day crustal deformation of continental China derived from GPS and its tectonic implications. *J. Geophys. Res. Solid Earth* **2020**, *125*, e2019JB018774. [CrossRef]
43. Chen, F.C.; Guo, L.Q.; Zhang, Z.J. Research on activity of Zhangjiakou-Bohai fault zone based on GPS observations. *Seismol. Geol.* **2020**, *42*, 95–108.
44. Yang, B.; Zhan, W.; Liu, Z.G. Basic characteristic and dynamic change of horizontal tectonic motion in Shanxi-Hebei-Inner mongolia area. *J. Seismol. Res.* **2013**, *36*, 472–477.
45. Liu, R.C. Regional Tectonic Deformation Characteristics of Shanxi Rift and Strong Earthquake Geodynamic Implications. Ph.D. Thesis, Taiyuan University of Technology, Taiyuan, China, 2022.
46. Wang, X.; Song, M.Q.; Wu, H.Y.; Liang, X.J.; Lv, R.; Guo, W.F.; Zhang, N.; Li, J. Stress field in Shanxi rift and its dynamic significance. *Seismol. Geol.* **2026**, *48*, 257–277.
47. Lin, X.D.; Yuan, H.Y.; Xu, P.; Yang, X.; Xu, Z.G.; Sun, H.X.; Hou, L.J.; Xu, S.T.; Xi, C.X. Zonational characteristics of earthquake focal mechanism solutions in North China. *Chin. J. Geophys.* **2017**, *60*, 4589–4622. (In Chinese)
48. Bi, J.M.; Song, C.; Ma, Y. Segmentation of seismicity characteristics along the Zhangjiakou-Bohai tectonic belt. *China Earthq. Eng. J.* **2025**, *47*, 1232–1242.
49. Liao, C.T.; Zhang, C.S.; Wu, M.L.; Ma, Y.S.; Ou, M.Y. Stress change near the Kunlun fault before and after the Ms8.1 Kunlun earthquake. *Geophys. Res. Lett.* **2003**, *30*, 2027. [CrossRef]
50. Guo, Q.L.; Wang, C.H.; Ma, H.S.; Wang, C.G. In-Situ hydro-fracture stress measurement before and after the Wenchuan Ms8.0 earthquake of China. *Chin. J. Geophys.* **2009**, *52*, 1395–1401.


**Disclaimer/Publisher's Note:** The statements, opinions and data contained in all publications are solely those of the individual author(s) and contributor(s) and not of MDPI and/or the editor(s). MDPI and/or the editor(s) disclaim responsibility for any injury to people or property resulting from any ideas, methods, instructions or products referred to in the content.